Digital sand core physics: Predicting physical properties of sand cores by simulations on digital microstructures

Florian Ettemeyer[a], Philipp Lechner[b], Tobias Hofmann[c], Heiko Andrä[c], Matti Schneider[d,*], Dominik Grund[a], Wolfram Volk[a,b], Daniel Günther[a]

[a] *Fraunhofer Research Institution for Casting, Composite and Processing Technology (IGCV), Germany*
[b] *Technical University of Munich, Chair of Metal Forming and Casting, Germany*
[c] *Fraunhofer Institute for Industrial Mathematics (ITWM), Department of Flow and Materials simulation, Germany*
[d] *Karlsruhe Institute of Technology (KIT), Institute for Engineering Mechanics, Germany*

1. Introduction

Fabricating sand-cores for metal castings is an established and economically viable process for manufacturing via molding of complex shapes (Rao, 1996). Still, the connection between various parameters, such as the sand type, chemical properties, amount of binder and the molding process, and the quality of the final sand core is still not well-established, relying upon tedious calibration, expert's knowledge and, typically, several iterations. Understanding and predicting the physical properties strength, permeability and thermal conductivity from geometric parameters is expected to accelerate the development process and to aid the transition from the conventional tool-based production to additive manufacturing of sand-cores.

We rely upon a multi-scale approach for gaining a deeper understanding of sand core microstructures, as is standard for other material classes, such as metals (Feyel and Chaboche, 2000), particle reinforced composites (Köbler et al., 2018) and rocks (Andrä et al., 2013a; 2013b). This so-called digital sand core physics shall start from the individual sand grains, taking into account the complex binder network connecting the individual sand grains and eventually set up a full simulation chain for computing the effec-

* Corresponding author.
E-mail address: matti.schneider@kit.edu (M. Schneider).

tive physical properties of interest from characteristics of the sand and binder used.

1.1. State of the art

Modeling and simulation of rock physics serves as a source of inspiration for the microstructural investigations performed in this study. Experimental results for the properties for silicate glasses in homogeneous state are available (Martinsen, 1969). Models for rock fracture (Perras and Diederichs, 2014; Coviello et al., 2005) or multi-physical properties (Mavko et al., 2009; Provis et al., 2009) as well as theoretical investigations for the binder phase (Polzin, 2013) or modeling of the casting process (Vergnano et al., 2019) can be found in the literature. However, we did not find a complete model for macroscopic investigations based on computer-generated grain agglomerates.

There are different approaches for the microstructure modeling of agglomerates. Approaches based on Voronoi tesselations, like in Schüler et al. (2016), suffer from two shortcomings. Firstly, prescribing the grain shape is difficult, because this shape is a result of the tesselation. Rather, the seed points (and weights for Laguerre tesselations) need to be prescribed, and the connection to the final shapes is non-trivial. Secondly, the resulting microstructures are not mechanically stable, because the modeling is explicit.

In contrast, approaches based on the DEM (discrete element method) using a description of the grains either by polyhedra (Cundall, 1988a; 1988b) or non-overlapping spheres (O'Sullivan, 2011; Das, 2007) ensure mechanical stability by heaping up individual sand grains until the final (stable) configuration is reached. However, the speed (and, thus, the usefulness) of the DEM is closely tied to the complexity of the particle description. Thus, particular approaches for modeling the shape of sand grains accurately, see (Mollon and Zhao, 2012; 2014), are incompatible to large scale DEM simulations. A compromise was found in Schneider et al. (2018), where particles of complex shape are represented by clusters of overlapping spheres, leading to a fast collision detection for particles of complex shape. The latter work is also the starting point for the investigations of this article.

The thermal conductivity of several minerals has been analyzed extensively in Horai and Simmons (1971). Furthermore, the influence of grain size on the thermal conductivity of a composite material has been investigated in Woodside and Messmer (1961) and Midttomme and Roaldset (1998). Chen (2008) and Zych et al. (2015) conducted experimental studies on the thermal conductivity, especially of sand and binders. These studies laid their focus on the mineral models, with a transfer to applied questions like the casting process missing yet.

For gas permeability in casting forms only few contributions exist. For practical investigations a test rig was proposed by Reuß and Ratke (2010). The connection to the inner geometric structure of the material is disregarded by the state of the art.

While the linear elastic properties of sand core materials have been intensively analyzed in Schneider et al. (2018), this work tries to extend the model by including damage effects in order to predict the mechanical strength. Due to similarity of the fracture behavior of bound sand to concrete failure (Grassl and Jirásek, 2006) or rock fracture (Shanthraj et al., 2017), such models can also been applied to sand core materials (Provis et al., 2009). The mechanical behavior of the binder water-glass, on the other hand, will be defined in this study with a damage model inspired by ones successfully used for steel-reinforced-concrete (Lubliner et al., 1989) and glass-fiber-reinforced-polymers (Spahn et al., 2014). It was originally developed and applied for rock physics (Andrä et al., 2013a). In the literature no hint can be found how the statistics of the fracture mechanics can be explained on consideration on the microscale. The study claims to disclose a new approach to explain these characteristics statistically.

1.2. Design of this study

In this work we investigate computer simulations to obtain effective physical properties from digital microstructures, and compare these to corresponding experiments. More precisely, the physical properties under consideration are the most relevant for the casting process: thermal conductivity, permeability and strength. For the microstructures, we use both X-ray micro-computed tomography (μCT) images and computer generated microstructures. Unfortunately, for strength simulations, we cannot solely rely upon μCT images because the binder cannot be separated from the sand grains by imaging techniques because of the similarity in absorption rate of binder and sand.

Typically, sand cores consist of natural sand, for example silica sand (Quartz Sand Haltern plant H31 - H35; Foundry sands). For special purposes, artificial sands, like bauxit-sand type W65, are employed. W65 sand consists mainly of Al_20_3 and has its melting point at 1820 °C (Recknagel and Dahlmann). Because of their frequent usage in the casting industry, this study considers the three sand types H32, GS14 and W65. In addition to the sand grains, a binding agent is added for connecting the grains to finally form the sand core. This study focuses on sand cores bound by water glass because of their potential to increasing sustainability and eco-friendliness of the casting process.

We extend the microstructure generation method of Schneider et al. (2018) two-fold. Firstly, we utilize high-fidelity representations of the individual sand grains to dispense with the time-consuming morphological dilation that was necessary in Schneider et al. (2018). More precisely, the representation of the grains by clusters of overlapping spheres led to a bumpy surface which had to be corrected by using mathematical morphological operations. Secondly, we conduct an additional μCT scan of unbound sand, together with modern image processing tools, to identify volumetric representations of over 1000 different sand grains. Up to the resolution of the μCT-scan (and issues of segmentation), these volumetric images exactly represent the shape of the sand grains. In particular, our approach goes beyond classical two- and three-dimensional shape descriptors which are used, aided by two- and three-dimensional imaging techniques, for characterizing the sand. For instance, we get more refined data than available by a classical sieve analysis. Due to the anisotropy of the sand grains, results of the sieve analysis may be random. In contrast, we have the full volumetric description at our disposal.

With these high-fidelity microstructures at hand, we set up simulation scenarios for computing the effective thermal conductivity, effective permeability, and the effective strength of bound sand with state-of-the-art solvers specialized for large scale regular voxel data, cf. Section 2. The numerical treatment is complemented by dedicated experiments, cf. Section 3, where we specify the image analysis methods and the experimental techniques. Finally, the experimental and numerical results are presented in Section 4, augmented by interpretation and evaluation of the data. Each of these three sections is divided into the subsections volume composition, thermal property analysis, permeability analysis and mechanical properties analysis. The key findings are wrapped up in the conclusions section.

2. Simulation setup

This section gives an overview of the simulation approaches as well as the equations to be solved for thermal transport, gas permeability and the damage mechanics of bound sand.

(a) 1/64th of a μCT image, with 59.04% sand and binder (cannot be separated)

(b) Computer-generated volume element with 58.55% sand (grey) and 1.5% binder (black)

Fig. 1. Visual comparison of μCT data and a computer-generated volume element for H32 sand.

2.1. Volume composition - Generation of volume elements

As the basic computational domains for our simulations we rely upon

1. X-ray micro-computed tomography (μCT) data of bound sand,
2. computer-generated digital volume elements of sand cores.

Modern μCT techniques permit a detailed three-dimensional characterization of bound sand after casting. However, due to similarity in absorption rate, binder and sand grains cannot be distinguished on such an image. Still, these geometries can be used for permeability analysis and also for calibrating the computer-generated volume elements. The latter was carried out in Schneider et al. (2018), where the μCT-data of bound sand we are using in this work originates from.

To model the sand and binder phases separately, we improve upon the method introduced in Schneider et al. (2018), which works as follows. Three-dimensional volumetric images of individual sand grains serve as the basic input. With the total number of grains fixed, different types of grains are rescaled and mixed, depending on the grain size distribution (either known from the spec sheet or determined by a sieve analysis). Then, these grains are randomly distributed into a large volume, which is subsequently compressed, accounting for inter-grain contacts, until the desired volume fraction (about 62%) is reached. For the collision detection, the individual grains were approximated by a rigid cluster of overlapping spheres. Once the grains have reached their final position, they are rescaled to the target volume fraction (about 58.55%). In a final step, binder is added by morphological operations (also, with the correct volume fraction of about 0.7%).

For this work, the latter procedure was improved in two ways. In Schneider et al. (2018), the individual sand grains needed to be segmented by hand, resulting in a low variety of possible grain shapes. In this work, we conduct μCT scans of unbound sand, which enable modern image processing techniques to identify almost all sand grains within the sample, leading to a large variety of known sand grain shapes. The procedure is detailed in Section 3.2. Relying upon real sand grain shapes obtained by μCT analysis is a crucial technological advance. Classically, a set of shape descriptors is chosen which "characterize" the sand grains, e.g. Fourier descriptors (Mollon and Zhao, 2012; 2014) or geometric characteristics (Das, 2007). Here, characterization is just an euphemism for measurement. It is by no means clear that these shape descriptors uniquely characterize the sand grain's physical behavior. We circumvent the latter immensely difficult question by working on the individual sand grains themselves. Of course, not all characteristics are captured (like surface roughness or pre-fractured areas). Still, a large source of uncertainty is eliminated that way.

The second improvement concerns the volumetric description of the sand grains. In Schneider et al. (2018), after the compression procedure, the sand grains were voxelized based on their representation by a cluster of overlapping spheres. To rectify the artificially introduced bumpiness, morphological operations were used. In contrast, we rely upon a description of the sand grains either by a CAD model or a high-resolution voxel image. Indeed, upon rescaling and compression, the initial sand grain differs from the final configuration by an affine motion $x \mapsto Qx + b$, that is the composition of an isotropic dilation and an Euclidean transformation. The latter affine transformation is applied to the original CAD or voxel model to transfer a highly detailed sand grain description to the generated sand core.

In Fig. 1, an example of a μCT image and a computer-generated structure are shown. In terms of complexity, both structures are comparable. For the computer-generated structures, binder and sand grains can be separated. On the μCT image, the defects within the sand grains are clearly visible. Comparing the structures in a more quantitative fashion, i.e. in terms of their effective physical properties, led to this article.

For the microstructure generation, grain size data was taken from the sieve analysis of the different sands according to their respective spec sheets (Quartz Sand Haltern plant H31 - H35; Foundry sands; Recknagel and Dahlmann). The binder volume fractions were chosen from the 0.5% to 2% in 0.5% steps, which is close to real casting conditions. For studying the influence of the underlying numerical resolution, three different voxel counts were chosen: 128^3, 256^3 and 512^3. For each structure, the grain sizes were chosen quasi-randomly and according to the sieve analysis of the sand. The number of grains was specified to $5^3 = 125$, which was found representative in Schneider et al. (2018). As all structures were compressed to one and the same volume fraction of

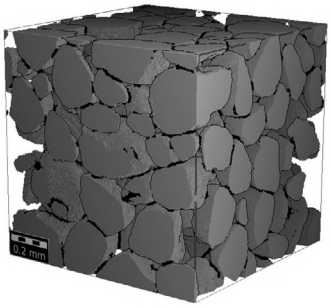

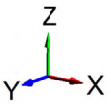

(a) Computer-generated microstructure of H32 sand with 58.58% sand and 1.5% binder

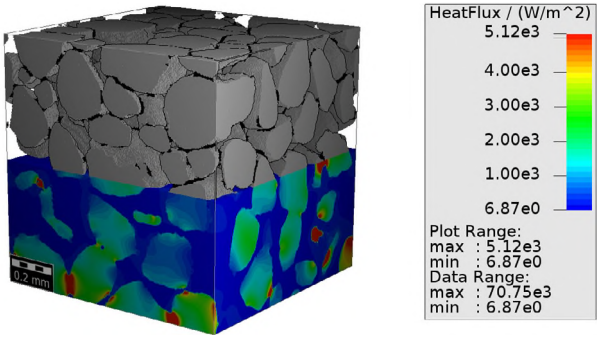

(b) Computed local heat flux for a temperature difference of 2°C in x-direction

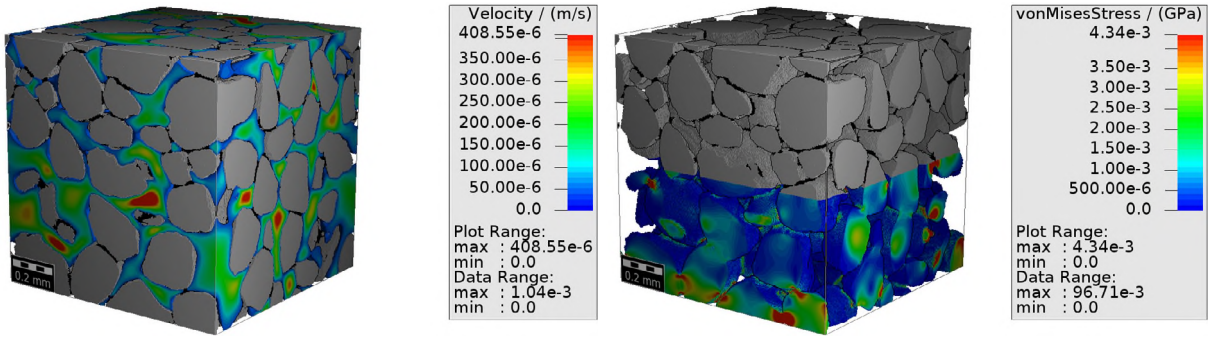

(c) Magnitude of the computed velocity field for a pressure drop of 0.02Pa in x-direction

(d) Compute von Mises equivalent stress field for 0.005% applied strain in x-direction

Fig. 2. Simulation portfolio: computing thermal conductivity, permeability and the elastic tensor for a single grain-binder aggregate.

58.55%, the representative volume element varied slightly in size, from 370 to 385 µm. To introduce stochastic effects in our model, for each parameter set ten virtual realizations were generated. This resulted in a total of

$$3\,\text{sieve lines} \times 4\,\text{binder vol. frac.} \times 3\,\text{disc.} \times 10\,\text{Reals.} = 360\ \text{microstructures}. \tag{1}$$

If not mentioned otherwise, each of the microstructure simulations was conducted for all ten realizations, and the resulting mean value was reported.

Due to the experimental boundary conditions for measuring the thermal conductivity, the specimens were crushed. To account for this effect, the virtual specimens were modeled as a powder form without binder. These models are called “virtually re-grained” in this article.

2.2. Thermal property analysis

During casting, both the inserted sand cores and the casting forms are heated up rapidly. The mechanical properties of the casting part are mainly controlled by the thermal conductivity. A higher cooling rate of the casting part corresponds to a finer grain size in the microstructure of the casting part, which in turn leads to an improved mechanical strength. Therefore, detailed knowledge of the temperature conditions vs. time and, in particular, the thermal conductivity during casting are of special interest.

Suppose a microstructure $Y \subseteq \mathbb{R}^3$ is given, together with a microscopic field of isotropic thermal conductivities $\lambda : Y \to \mathbb{R}$ (measured in $\mathrm{W\,m^{-1}\,K^{-1}}$). For our application, λ takes three different values, one for each of the three constiuents. To compute the effective thermal conductivity tensor, three linear experiments need to be solved. More precisely, we seek, for $i = 1, 2, 3$, a periodic temperature fluctuation field $\theta_i : Y \to \mathbb{R}$, s.t. the microscopic static heat equation

$$0 = \vec{\nabla} \cdot \lambda(\vec{e}_i + \vec{\nabla}\theta_i), \tag{2}$$

where $\vec{e}_i$ denotes the unit vector in the i-th coordinate direction, is satisfied. Then, the effective thermal conductivity tensor is calculated by the Fourier-type law

$$\lambda_{ij}^{\text{eff}} = -\vec{e}_j \cdot \langle \lambda(\vec{e}_i + \vec{\nabla}\theta_i) \rangle_Y,$$

where $\langle \cdot \rangle_Y$ denotes taking mean values. The static heat Eq. (2) is discretized on a regular voxel grid by a finite volume scheme and solved by the EJ-HEAT method, as outlined in Wiegmann and Zemitis (2006) and implemented in the ConductoDict module of GeoDict (2019). A typical result of such a simulation can be seen in Fig. 2(b).

2.3. Permeability analysis

During casting the metal is flowing fast into the cavity through the gating system. During this process, air can be entrapped and moved by the melt front. If the gating has more than one opening towards the cavity, several melt fronts can coalesce, creating gas bubbles in the finally solidified part. A second source of such defects is gas generated under heat influence, for example by the humidity present inside the cores. To minimize such defects in the casting part, gas should flow through the sand core and run out through the core marks instead of leaking into the melt.

Stokes’ model for incompressible fluids with constant density is suitable for describing the air-flow through the porous structure. Of primary interest is the pore space Ω within the computational box Y. To compute the effective permeability, for $i = 1, 2, 3$, a periodic velocity field $\vec{v}_i : \Omega \to \mathbb{R}^3$ and a periodic pressure field

Table 1
Young's modulus and Poisson's ratio for the sand and the binder according to Schneider et al. (2018).

	H32 sand	Water glass binder
E	66.9 GPa	71.7 GPa
ν	0.25	0.17

$p_i : \Omega \to \mathbb{R}$ are sought solving the system of equations

$$\begin{aligned} \mu \Delta \vec{v}_i + \vec{\nabla} p_i &= -\vec{e}_i \quad \text{in } \Omega, \\ \vec{\nabla} \cdot \vec{v}_i &= 0 \quad \text{in } \Omega, \\ \vec{v} &= 0 \quad \text{on } \partial\Omega. \end{aligned} \tag{3}$$

These equations encode balance of linear momentum, mass conservation and the no-slip boundary condition along the "inner" boundary, disregarding parts on Y. Then, the effective permeability is computed from

$$\kappa_{ij}^{\text{eff}} = -\frac{1}{\mu} \vec{e}_j \cdot \langle \vec{v}_i \rangle_Y. \tag{4}$$

Notice that the shear viscosity μ enters linearly in (3), and inversely in (4). Thus, the effective permeability is independent of the viscosity μ, and is completely determined by the geometric distribution of the porous phase Ω within the cell Y.

The Stokes system (3), together with the no-slip boundary conditions, is discretized by a finite volume method (Wiegmann, 2007) and solved by the LIR solver (Linden et al., 2015) implemented in the FlowDict module of GeoDict 2019. A typical result of such a simulation can be seen in Fig. 2(c).

2.4. Mechanical property analysis

The strength of the blown sand cores is of principal interest for casting applications, as too low strength may lead to failure of the core during casting, and too high strength exacerbates extracting the final casting. Thus, the choice of sand, binder and processing conditions for manufactoring sand cores needs to be taylored to yield sand cores with a strength lying in this narrow window.

To gain deeper insight into the relationship between the sand core microstructure, where we can control a variety of parameters such as volume fractions and grain size distribution, and the resulting fracture mechanical parameters of the blown material, we conduct simulations on appropriate microstructure models of the sand-binder aggregate.

Sand cores are known to behave in an almost perfectly brittle way (Griebel et al., 2016), i.e. the material behavior is linear elastic until the critical strain is reached. Upon reaching this strain, the material fails suddenly in a brittle way. Furthermore, sand cores exhibit a strong tension-compression anisotropy, i.e. when subjected to tensile loading, the material fails at extremely low strain levels, whereas when compressed, the material is able to withstand much higher strain levels until final failure.

In the previous subsections, only the distinction between pore space and solid material was needed. For mechnics, the scope of the investigations requires a more detailed description. The pore space does not contribute to the mechanical stability of the structure at all. Thus, its elastic properties are set to zero. Whereas the sand grains are assumed as a solid material with a maximum fracture stress above the level considered in this work, the binder is considered to be much more fragile. We have seen in a previous study (Schneider et al., 2018), where both binder and sand grains were modeled as linear elastic, that the highest strains are reached in the binder regions. Thus, the sand material is modeled as linear elastic, cf. Table 1, and the binder obeys an isotropic damaged material law with initial elastic domain. The isotropic linear elastic parameters of the binder are collected in Table 1. The stress field within the binder is given by an isotropic local damage model

$$\boldsymbol{\sigma} = (1-d)\mathbb{C} : \boldsymbol{\varepsilon} \tag{5}$$

where $\boldsymbol{\varepsilon}$ is the strain field, $\mathbb{C}$ stands for the linear elastic tensor and the damage variable d is driven by

$$d(\vec{x}, t) = \min\{\max\{f(\tilde{\varepsilon}(\vec{x})), \max_{0 \le \tau \le t} d(\vec{x}, \tau)\}, d_{\max}\}, \tag{6}$$

i.e. the damage value is bounded from below by its maximum past value, and bounded from above by a maximum threshold value.

The latter evolution involves an equivalent scalar strain measure $\tilde{\varepsilon}(\vec{x})$, to be determined below, and a damage degradation function f, following (Mazars and Pijaudier-Cabot, 1989), defined by

$$f(\tilde{\varepsilon}) = \begin{cases} 0 & \text{if } \tilde{\varepsilon} < \tilde{\varepsilon}_0, \\ 1 - \frac{\tilde{\varepsilon}_0}{\tilde{\varepsilon}}(1-\alpha) - \alpha \exp[-\beta(\tilde{\varepsilon} - \tilde{\varepsilon}_0)] & \text{otherwise.} \end{cases} \tag{7}$$

For this model, which is conventionally used for modeling concrete, the material remains intact unless a value of $\tilde{\varepsilon}_0$ is reached. For higher $\tilde{\varepsilon}$, the damage value increases monotonically with exponential rate subject to $f(\tilde{\varepsilon}) \nearrow 1$ as $\tilde{\varepsilon} \to +\infty$. Notice, however, that the maximum value of damage is constrained to $d_{\max}$ by (6). Furthermore, due to the history-dependence in (6), the damage evolution is irreversible.

It remains to specify the form of the equivalent strain measure $\tilde{\varepsilon}$ as a function of the strain tensor $\boldsymbol{\varepsilon}$. To take into account the different behavior of brittle materials when subjected to tension and compression, respectively, we follow the suggestion of de Vree et al. (1995) and define

$$\tilde{\varepsilon} = f_1 I_1 + f_2 \sqrt{f_3 I_1^2 + f_4 J_2'} \tag{8}$$

where

$$I_1 = \operatorname{tr}(\boldsymbol{\varepsilon}) \quad \text{and} \quad J_2' = \frac{1}{2} \left\| \boldsymbol{\varepsilon} - \frac{1}{3} \operatorname{tr}(\boldsymbol{\varepsilon}) \operatorname{Id} \right\|^2,$$

denote appropriate invariants of the strain tensor involving the Frobenian norm $\|S\|^2 = \operatorname{tr}(S^T S)$ and

$$f_1 = \frac{\gamma - 1}{2\gamma(1-2\nu)}, \quad f_2 = \frac{1}{2\gamma}, \quad f_3 = \frac{(\gamma-1)^2}{(1-2\nu)^2}, \quad f_4 = \frac{12\gamma}{(1+\nu)^2},$$

denote shape factors depending on the Poisson's ratio of the material and the ratio of tensile and compressive strength $\gamma \in [1, \infty)$.

Thus, the entire damage model involves - in addition to the linear elastic moduli - only four adjustable parameters, whose values are specified in Table 2.

Table 2
Damage parameters for water glass, cf. Section 4.4.

γ	$\tilde{\varepsilon}_0$	$d_{\max}$	α	β
3	10^{-4}	0.98	0.98	282

For computations on the unit cell $Y \subseteq \mathbb{R}^3$ and given macroscopic strain $E : [0, t_{\max}] \to \mathbb{R}^{3\times3}_{\text{sym}}$ we seek a microscopic displacement fluctuation

$$\vec{u} : Y \times [0, t_{\max}] \to \mathbb{R}^3$$

and a damage field

$$d : Y \times [0, t_{\max}] \to \mathbb{R},$$

s.t. the (quasi-static) balance of linear momentum

$$\vec{\nabla} \cdot \boldsymbol{\sigma}(x, t) = 0, \quad x \in Y, \quad 0 \le t \le t_{\max},$$

is satisfied, where the stress field

$$\boldsymbol{\sigma} : Y \times [0, t_{\max}] \to \mathbb{R}^{3\times3}_{\text{sym}}$$

is given by the constitutive law within the respective phases, i.e.

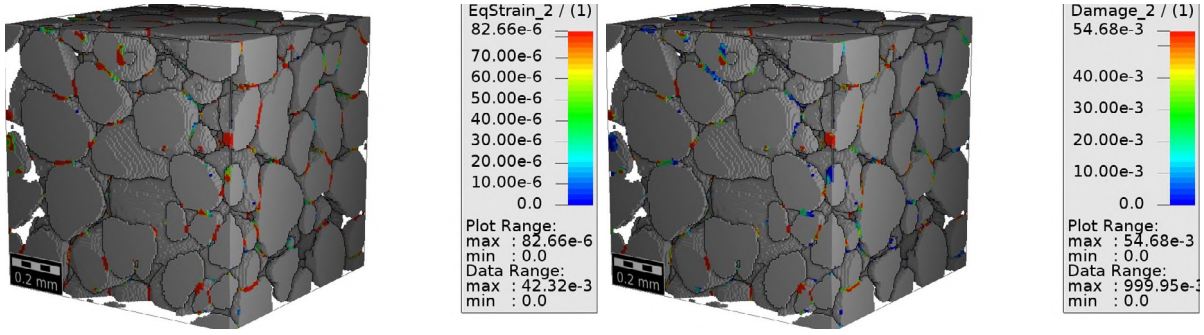

(a) Equivalent strain $\tilde{\varepsilon}$, cf. (8). (b) Damage variable d, cf (6).

Fig. 3. Equivalent strain measure and damage distribution for uniaxial extension in x-direction and $\beta = 280$ resulting from one of the computations of Section 4.4.

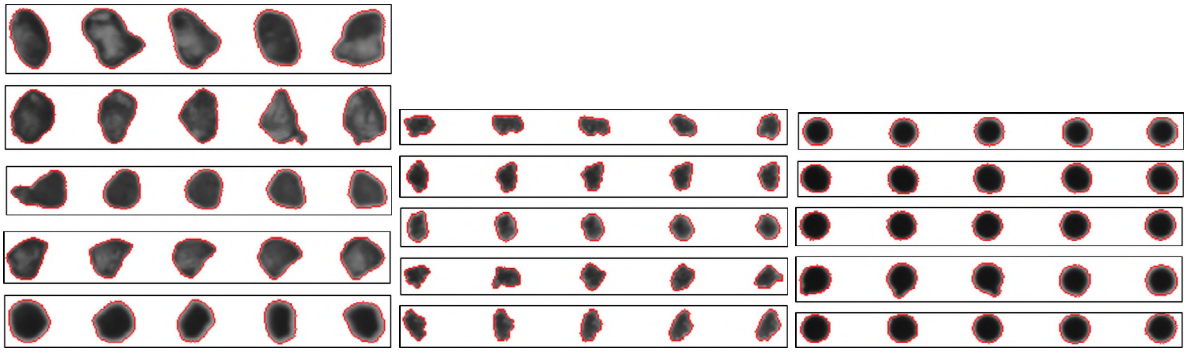

(a) H32 silica sand $d50 = 320\mu m$ (b) GS14 silica sand $d50 = 140\mu m$ (c) W65 bauxit sand $d50 = 150\mu m$

Fig. 4. Micrographs of different sand types, including the mean diameter $d50$. Within every box, the same sand grain is shown, photographed from different angles. Different boxes show different sand grains.

1. $\boldsymbol{\sigma}(x,t) = 0$ if x lies in the pore space,
2. $\boldsymbol{\sigma}(x,t) = \mathbb{C}^{sand} : \boldsymbol{\varepsilon}$ if x lies within the sand grains,
3. $\boldsymbol{\sigma}(x,t) = (1 - d(x,t))\mathbb{C}^{binder} : \boldsymbol{\varepsilon}$ if x lies in the binder region, and the evolution of damage is governed by the model following equation (5),

where $\boldsymbol{\varepsilon}(x,t) = E + \frac{1}{2}(\vec{\nabla}\vec{u}(x,t) + \vec{\nabla}\vec{u}(x,t)^T)$ denotes the total strain. The effective stress is computed by volume-averaging $\boldsymbol{\sigma}(t) = \langle \boldsymbol{\sigma}(\cdot,t) \rangle_Y$.

The balance of linear momentum is discretized on a regular voxel grid, and solved by FFT-based computational micromechanics, where the kinetic equations for the evolution of damage are discretized in time by a backward Euler discretization and solved for any voxel, see (Spahn et al., 2014) for details. For the implementation we rely upon the ElastoDict module of GeoDict 2019.

A typical result of a linear elastic simulation can be seen in Fig. 2(d). For the damage model, in Fig. 3 the distribution of the equivalent strain and the damage variable in the binder phase is shown.

3. Setup for experimental investigations

This section specifies the physical test procedures, the equipment and the parameters. We start off with detailing the preparation of the test specimens, serving as the foundation for the subsequent investigations.

3.1. Preparation of the sand test specimens

For the experimental investigations, inorganically bound sand core specimens are used. These cores were produced by a Loramendi core-shooting machine with a shooting volume of 25 liters (Loramendi SLC-25L) and by a Voxeljet VX500 3D-printer.

Our investigations rely upon two different specimen geometries. The first geometry is a bar-shaped specimen with a quadratic cross-section, with an edge length of 22.4 mm and a length of 170 mm. The second geometry is cylindrical, where both the diameter and the height equal 50 mm.

Three different types of sand are used for the experimental investigations. Specimen type A is produced by core-shooting with silica-sand H32 from Quarzwerke Haltern, with a mean diameter of 320µm and 2*wt*% water glass fluid binder and 1.9*wt*% silicate additive. Specimen A is produced in both available shape, bars and cylinders. Specimen type B is also produced by core-shooting in shape of cylinders using W65 sand and an amount of binder and additive that is identical to specimen A. Specimen type C is produced by 3D-printing in shape of cylinders with GS14 silica sand from Quarzwerke Strobel with a mean diameter of 140μm as base material. As binder a water glass based solution with a solid content of 30% by weight is used.

In Fig. 4 typical shapes of the investigated sands are shown, measured by the optical measurement device PartAn3D from Microtrac. A qualitative comparison shows differences in both mean diameter $d50$ and roundness factor of the sands. Whereas the natural sands H32 and GS14 are characterized by sharp fracture edges of individual sand grains, the artificially produced W65 exhibits a higher degree of roundness. Details about the specimens and its production recipes are gathered in Table 3.

3.2. Volume composition - 3D image analysis

To complement the two-dimensional shape analysis of the sand grains, cf. Fig 4, we identify three-dimensional volumetric representations of individual sand grains. In a previous study (Schneider et al., 2018), micro-computed tomography (μCT) scans of the sand-binder-aggregate was performed. However, although

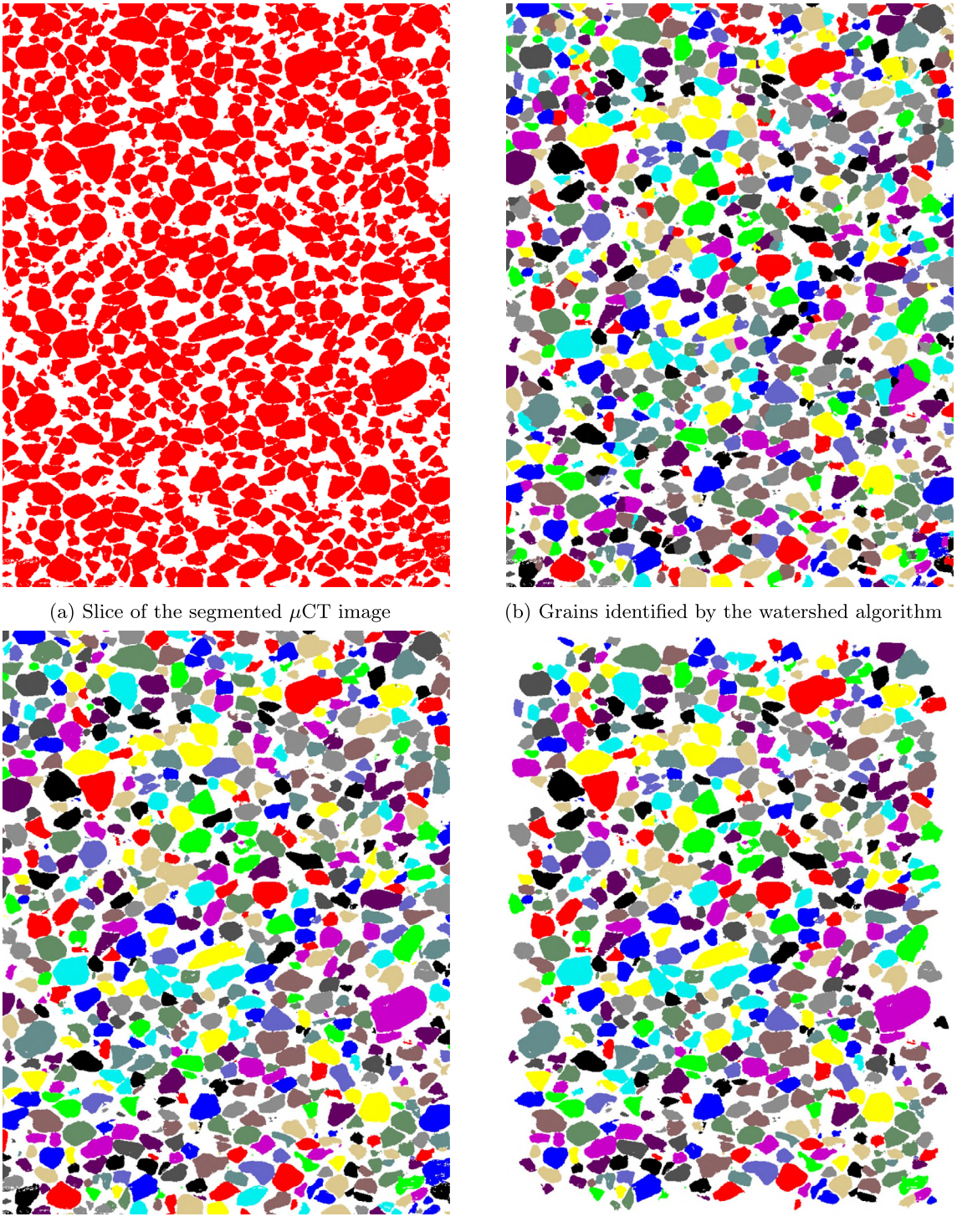

(a) Slice of the segmented μCT image

(b) Grains identified by the watershed algorithm

(c) After reconnecting fragmented grains

(d) After removing incomplete boundary grains

Fig. 5. Illustration of the image processing steps for segmenting individual sand grains.

the contrast between solid and pores is large enough to distinguish these phases, due to the similar absorption rates of sand grains and binder, the individual sand grains could not be separated from the binder easily. Only by a tedious manual identification procedure, a few individual sand grains could be identified.

For this work, we chose to dispense with the binding phase for the grain identification altogether, i.e. we investigate unbound sand which is heaped up in a containing box. More precisely, a μCT scan with a resolution of 4μm per voxel was carried out for the silica sand H32, resulting, after segmentation, in a $1500 \times 1500 \times 2000$ voxel image, cf. Fig. 5(b) for a cross section view.

Subsequently, a granulometric analysis was carried out. We use the method described in Tek et al. (2005) and Redenbach et al. (2014) for separating touching particles, combining the Euclidean distance transform (Maurer et al., 2003) with the watershed transform (Vincent and Soille, 1991). The algorithms, implemented in the Fraunhofer ITWM software MAVIkit (Fraunhofer ITWM, Department of Image Processing, 2005; 2009;

Table 3
Relevant parameters for production setup and the recipe of the specimens.

	specimen type A	specimen type B	specimen type C
production machine	core-shooting machine Loramendi SLC-25L		3D-Printer Voxeljet VX-500
used sand	H32	W65	GS14
recipe	$2wt\%$ water glass fluid binder and $1.9wt\%$ silicate additive		water glass based solution with a solid content of 30% by weight
shape	cylinder and bar	cylinder	cylinder

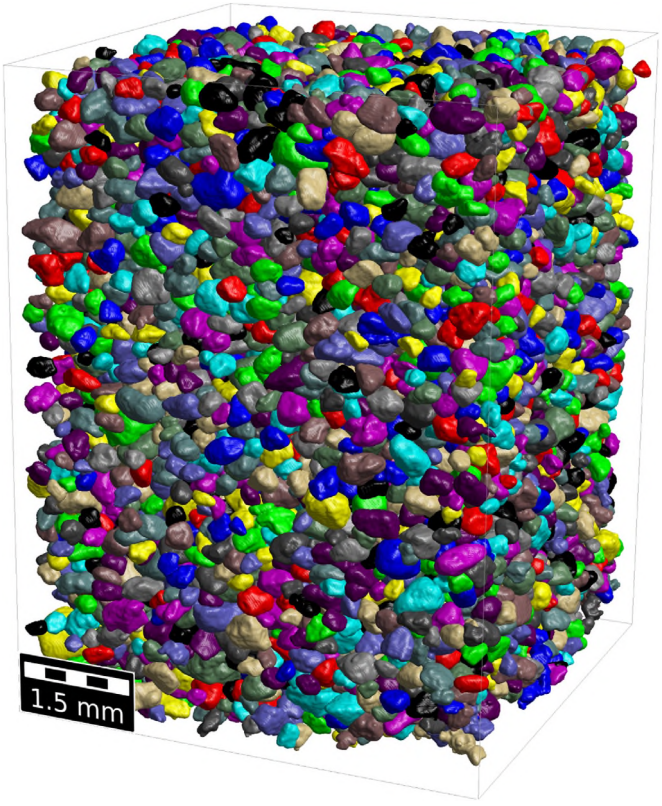

Fig. 6. 3D view of the identified sand grains.

2013), were used to segment 10590 grains. First, possible grains are identified by the classical watershed algorithm, see Fig. 5(b). The algorithm tends to overestimate the number of grains, i.e. a grain may be incorrectly fragmented by the algorithm. Thus, a heuristic re-connection algorithm is applied based on the expected sphericity of the grains. If the contact area relative to the volume of two grains is too large, they are reconnected into a single, larger grain, see Fig. 5(c). In a final step, sand grains intersecting the boundary are removed, see Fig. 5(d). A three-dimensional representation of the identified grains is shown in Fig. 6.

Care has to be taken, because the volume composition of bound sand may differ from the unbound case. For instance, for the unbound sand, very small particles may be ignored, distorting the overall grain size distribution. However, we use only the shape of the identified grains, scaling them properly to match the grain size distribution of the spec sheet. The previous study (Schneider et al., 2018) has shown that using this grain size distribution and the correct volume fractions of binder and sand grains lead to a good prediction of the effective elastic properties of the sand core composite.

3.3. Thermal property analysis

The simulations compute the effective thermal conductivity. To compare these results to experiments of the binder-sand aggregate, we make use of the relationship

$$\lambda(T) = a(T) \times \rho(T) \times c_p(T), \tag{9}$$

expressing the (temperature-dependent) thermal conductivity $\lambda(T)$ as a function of the specific heat capacity $c_p(T)$, the density $\rho(T)$ and the thermal diffusitivity $a(t)$.

For the specific heat capacity $c_p(T)$ we use differential scanning calometry (DSC), the density $\rho(T)$ is measured at room temperature with gaspycnometry and expansion coefficients are used from literature while the thermal diffusivity $a(T)$ is measured by laser flash analysis (LFA). Each method and the corresponding parameters will be described in the following.

3.3.1. Differential scanning calometry

To determine the specific heat capacity $c_p(T)$, measurements were conducted according to the sapphire method analogous to DIN 51007 on a Netzsch DSC 204 Phoenix. For the sapphire method, three measurements are performed with identical measuring programs. In a first step, the empty crucible is measured. Then, a sapphire sample with known course of the specific heat capacity is measured. In the final step, the same crucible is measured this time with the sample to be determined. The specific heat capacity of the sample is obtained by comparing the recorded DSC signals and correcting the crucible signal.

Aluminum crucibles with perforated lids were used as crucibles. The samples were available in granular form for the measurements in order to ensure appropriate dosing. The temperature program was a cycle from 0 to 600°C with a heating rate of $10K/min$ and an isothermal state both for the beginning and the end of the measurement. Nitrogen was used as the purge gas.

3.3.2. Thermo-mechanical analysis

To determine the density for the investigated temperature range, measurements with a gas pycnometer (Quantachrome Ultrapyc 1200) were conducted at room temperature with nitrogen as filling gas. For the temperature-related changes in density, the gradient of expansion was taken from Recknagel and Dahlmann. Those expansion coefficients were used to calculate the density by means of (10):

$$\rho(T) = \frac{\rho_0}{\left(1 + \frac{\Delta L}{L_0}(T)\right)^3}. \tag{10}$$

3.3.3. Laser flash analysis

The thermal diffusivity was determined in a Netzsch LFA 457 Micro Flash using a sapphire sample holder. The bottom side of the sample holder was affected by a laser pulse of 40ms at laser voltages between 2000 and 2300V. The temperature rise over time

Table 4
Relevant parameters for permeability.

Atmospheric pressure p_0 in Pa	Specimen diameter d in m	Reservoir volume of the test rig V_c in m^3	Through-flow specimen height h in m	Dynamic viscosity of air (Sutherland, 1893) μ in Pa s
9.662e4	5e-2	2.9e-3	5e-2	18.26e-6

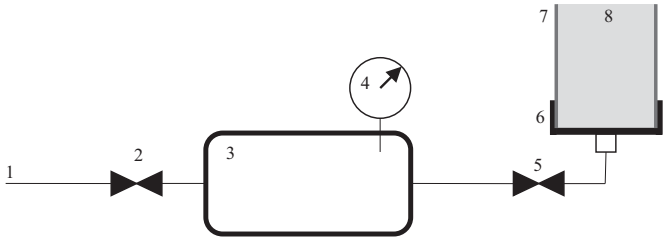

Fig. 7. Schematic of the test rig used for the permeability measurement.

was recorded on the top side by means of an IR detector. The thermal diffusivity was calculated from the half-life of the increase in the fit of the IR measurement signal. This was determined for a temperature range from room temperature to 800°C in steps of 50 K.

3.4. Permeability analysis

To characterize the gas permeability, we investigate the outflow of gas from a pressured specimen once the applied pressure is released instantaneously. This method is more robust compared to state of the art instruments, which measure a volume flow, and thus appropriate for fast use under rough conditions in industrial casting applications.

To interpret the measured data, an underlying modeling assumption is necessary. If the pore flow is modeled by Stokes' equation, a linear relationship between velocity and pressure difference is obtained, resulting in a constant permeability. For a flow modeled by the Navier-Stokes equation, velocity and pressure difference are related in a non-linear way, leading to a velocity-dependent permeability. In this section, we rely upon a linearized velocity-pressure difference relationship valid for small pressure differences.

A schematic of the test rig is shown in Fig. 7. An inorganically bound sand core (8) with a diameter and height equal to 50mm, as described in Section 3.1, is fixed via a clamping device (6) and sealed at the margin by a pneumatic collar (7). By opening valve 1 (2), the pressure tank (3) can be filled with air through the pressurized air supply (1) until the desired pressure in the tank is reached. By closing valve 1 and opening valve 2 (5), the air inside the tank can stream through the specimen and the time-dependent pressure loss in the tank is measured and recorded by a digital pressure gauge (4). The relevant parameters for the experimental investigations on the test rig are summarized in Table 4. With decreasing gas permeability of the specimen, the time to exhaust the tank is increasing.

In contrast to the work of Reuß and Ratke (2010), the test rig used in this article uses an excess pressure compressor instead of a vacuum pump to induce a gradient between the pressure in the test rig and the ambient pressure. The pressure in the pressure chamber can therefore be varied between ambient pressure and 7bar. In addition to allowing for a wider range of test scenarios, this setup is closer to the actual processing conditions during casting when gas flows out of the sand cores into the melt.

As a result, a time series of pressures inside the tank is recorded. For the following derivation, it is assumed that the air

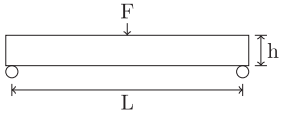

Fig. 8. Schematic of the three-point-bending-test used for measuring the mechanical strength.

leaves the pressure tank with the average velocity v at the outlet of the porous medium. Let ρ denote the density of the air inside the pressure tank. Then, the mass m equals density ρ times volume V_c. The mass change with time is then given as $\dot{m} = \dot{\rho} V_c$, as well as by the mass flow through the porous medium, $\dot{m} = \rho A v$, where $A = r^2\pi$ denotes the are of the cross-section. The outlet velocity can therefore be calculated from the pressure difference via

$$v = \frac{V_c}{A}\frac{\dot{p}}{p}. \tag{11}$$

The values acquired by the transformation can be compared with simulation results, as the average velocity is an observable quantity independent of the specimen thickness. Using this procedure, comparing to simulations on representative volume elements is sensible. Permeability can finally be calculated from the average flow speed by

$$K = \frac{Q\eta l}{A\Delta p} = \frac{Av\eta l}{A\Delta p} = \frac{v\eta l}{\Delta p}, \tag{12}$$

where Q denotes the flow rate in $m^3 s^{-1}$, η stands for the dynamic viscosity in Pa s, l is the length of the specimen in m, A refers to the cross-section in m^2 and Δp symbolizes the pressure difference in Pa. For air, the dynamic viscosity of $\eta = 18.26$ μPas is determined from Sutherland's formula (Sutherland, 1893). The permeability K has the standard units m^2, but is usually given in terms of Darcy with

$$1\text{D} = 9.86923 \cdot 10^{-13} \text{m}^2. \tag{13}$$

3.5. Mechanical property analysis

For measuring mechanical properties, bending experiments were performed. Due to the strongly brittle nature of sand cores, tensile experiments lack reproducibility.

As test specimen we use bending bars of dimensions 22.8 mm × 22.8 mm × 175 mm. We examine three-point bending, where the bearing positions are located in a distance of 150 mm relative to each other. The measurement force is applied on the top of the specimen, as shown in Fig. 8.

All measurements were performed on a universal testing machine type Zwick Z020 equipped with a 20kN force sensor. The bending test was performed with a feed rate of 1 mm/s. The start force is set to 20 N and the deflection is determined. Standard atmospheric conditions were used for these tests.

The maximum inner stress of loaded standardized specimens can be calculated from the macroscopic force for 3-point-bending by

$$\sigma = \frac{3FL}{2bh^2}. \tag{14}$$

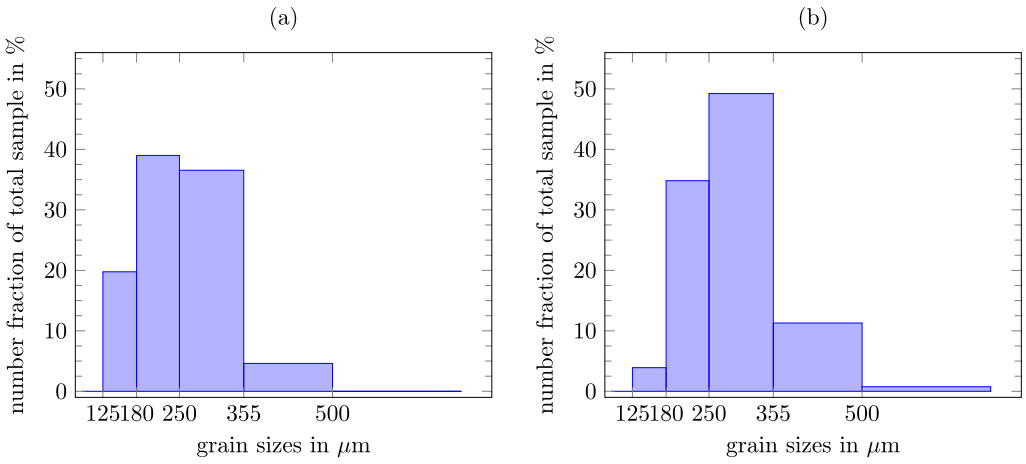

(a) According to the spec sheet[31]

(b) Determined from CT analysis

Fig. 9. Distribution of the grain diameter.

where F denotes the force and L, h and b stand for the length, height and width of the specimen, respectively, cf. Fig. 8.

Lechner et al. (2018) showed that the failure probability of the specimens, as a function of the applied stress σ, may be described by a Weibull distribution $W_{\sigma_N,m}$, i.e., the failure probability $p(\sigma)$ can be expressed in the form

$$p(\sigma) = 1 - \exp\left(-(\sigma/\sigma_N)^m\right), \tag{15}$$

where σ_N denotes the nominal strength (in units of stress) and the non-dimensional shape parameter m.

Given an ascending series $\{\sigma_1, \sigma_2, \ldots, \sigma_K\}$ of empirically obtained (scalar) failure stress values, the empirical failure probability is given by $p_i = p(\sigma_i) = \frac{i-\frac{1}{2}}{K}$. Then, Eq. (15) can be rewritten in the form

$$\begin{aligned} \log\left(-\log\left(1-p_i\right)\right) &= m\log\left(\sigma_i/1\text{MPa}\right) && -m\log\left(\sigma_N/1\text{MPa}\right), \\ y_i &= mx_i && -m\log\left(\sigma_N/1\text{MPa}\right), \end{aligned} \tag{16}$$

where the reference stress 1MPa was chosen to render the quotients $\sigma_i/1\text{MPa}$ and $\sigma_N/1\text{MPa}$ dimension-free, and the parameter pair (m, σ_N) is obtained by linear regression of the pairs

$$(x_i, y_i) = \left(\log\left(\frac{\sigma_i}{1\text{MPa}}\right), \log\left(-\log\left(1-p_i\right)\right)\right), \quad i = 1, \ldots, K. \tag{17}$$

The Weibull relationship (15) is only meaningful for a fixed volume and a homogeneous stress state. To account for the former, the relationship (15) needs to be extended (Danzer et al., 2007) to account for a homothetic change in volume

$$p(\sigma, V) = 1 - \exp\left(-(\sigma/\sigma_N)^m \frac{V}{V_0}\right). \tag{18}$$

Here, V_0 is a reference volume, and the quotient V/V_0 accounts for the well-known smaller-is-stronger effect observed in strength measurements. More precisely, the relationship (18) may also be interpreted as a change in nominal strength $\sigma_N \mapsto \sigma_N (V_0/V)^{\frac{1}{m}}$ upon a volume change $V_0 \mapsto V$. In this form, the decrease of the nominal strength upon increasing volume is apparent.

Furthermore, to account for a heterogeneous stress state, the relationship (18) needs to be further extended, cf. (Klein, 2009),

$$p(\sigma, V) = 1 - \exp\left(-\frac{1}{V_0}\int_V (\sigma/\sigma_N)^m \, dV\right). \tag{19}$$

4. Results

In this section, the results of the physical experiments and the simulations are presented, compared and discussed.

4.1. Volume composition - Sieve analysis

Fig. 9 compares the equivalent grain diameters of H32 sand according to the spec sheet (Quartz Sand Haltern plant H31 - H35) and determined from the CT analysis. Apparently, the CT-analysis detects fewer grains for the smallest diameters considered. This is caused by our way of measurement: we heaped up the sand grains for the CT scan. The tiny "dust" particles accumulate at the bottom of the domain of interest and are ignored by the image analysis. As the larger sand grains are responsible for the formation of the sand-binder microstructures, this is no problem, as the relative size of the three largest grain size bins is captured well.

After segmentation and cleansing the scanned volume was split into 64 equally-sized elements with dimensions $375 \times 375 \times 500$ voxels. As mentioned, these images cannot distinguish binder and sand phase. For this reason, they can only be directly used for the numerical simulation of permeability, as only the pore phase needs to be resolved. For both thermal property analysis and strength analysis, numerical simulation on digitally generated microstructures is inevitable.

4.2. Thermal property analysis

The DSC measurements of the specific heat capacities of the three investigated sands is shown in Fig. 10. Qualitatively, GS14 and H32 behave similarly except for an offset of approx. 0.3 to 0.5 J/(g·K). The specific heat capacities depend linearly on the temperature up to approx. 570°C, where a sharp peak manifests, which is caused by the transformation from low-temperature to high-temperature subpolymorphs taking place at 573°C for quartz (Pabst and Gregorová, 2013). In contrast, the specific heat capacity of W65 depends linearly on the temperature for the entire temperature range considered. Notice that the DSC furnace is limited to 600°C, in contrast to the LFA. This behavior is typical for the specific heat capacity, and is also observed in Wang et al. (2014) and Baumann and Zunft (2015). Whereas (Wang et al., 2014) report a heat capacity of 1.25 J/(g·K) at 50°C, Baumann and Zunft (2015) measure a heat capacity of 0.8 J/(g·K) at 50°C for silica sand. Our measurements tend to support (Baumann and Zunft, 2015). These authors also describe

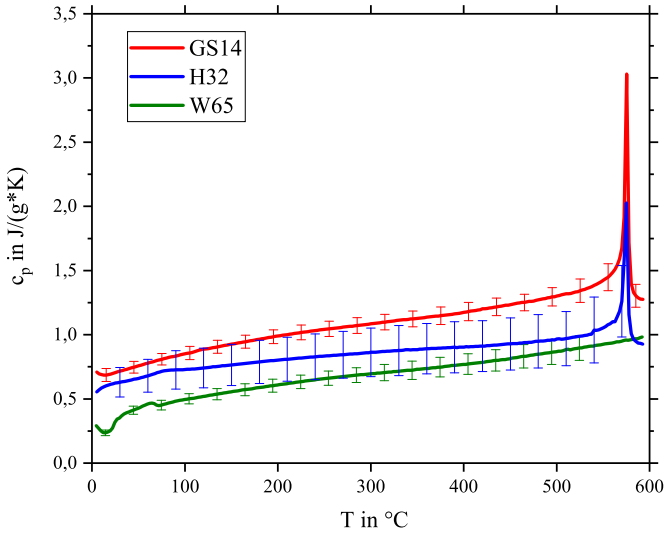

Fig. 10. Specific heat capacity vs. temperature.

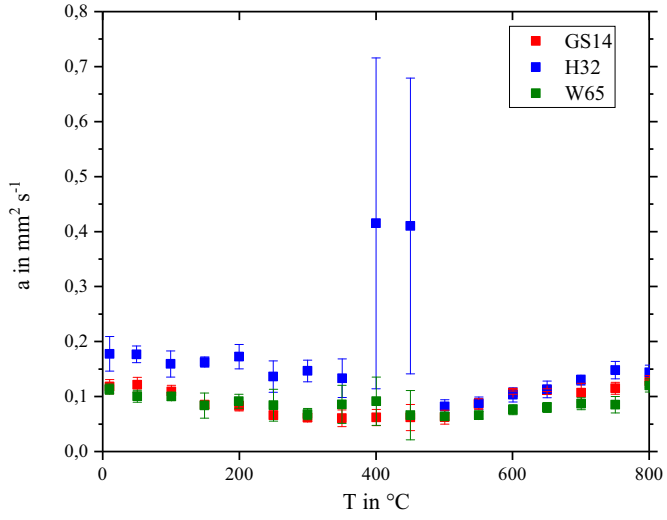

Fig. 11. Experimental results for the temperature diffusivity for the three investigated sands with error bars.

Table 5
Densities of the specimens at $T = 20°C$ and $T = 50°C$ in g/cm^3 with deviation.

Material	$\rho(20°C)$ in g/cm^3	$\rho(50°C)$ in g/cm^3	Deviation in %
GS14	2.6032	2.6001	0.12
H32	2.6309	2.6282	0.23
W65	6.2002	6.1964	0.28

that measuring the specific heat capacity may be influenced both by the compression of the granular medium and by the phase-composition of the silica sand-grains, explaining the differences in measured values between the mentioned articles.

The values for the thermal-dependence of the density were calculated using the change of length reported by Recknagel and Dahlmann. For H32, GS14 and W65 the results are shown in Table 5.

LFA measurements were conducted to determine the thermal diffusivity for the three investigated sand materials, cf. Fig. 11. The thermal diffusivity is a monotonically decreasing function of the temperature between 0°C and about 400 – 500°C. For higher temperatures, the thermal diffusivity increases, at least in the range up to 800°C.The decrease of the measured thermal diffusivities in the range 0 – 450°C is caused by the separated grains with a small contact surface at the beginning of the measurements which may be less conductive than the cavities, because the laser can shoot through the cavities directly to deeper layers and induce energy. As a result, initially a higher thermal conductivity of the specimens is measured. With increasing temperature and energy input of the laser, the cavities slowly become smaller due to expansion of the sand grains, and the impulses of the laser only reach the first layers of the sample under investigation. The energy must therefore be forwarded through the entire thickness of the specimen, leading to lower thermal diffusivities. The increase of the thermal diffusivity beyond 550°C is a result of the transformation from low- to high- quartz, where the crushed sand grains tend to expand and are, as a result, compressed stronger against each other. The thermal diffusivity of the sand W65, which does not exhibit a transformation, tends to be linear taking into account measurement uncertainties, supporting our interpretation. The measured peaks for sand H32 at 400°C are considered to be measurement errors with no need of further interpretation.

The thermal conductivity of the investigated sands can be determined as a function of the thermo-mechanical analysis, DSC and LFA measurement results, cf. Eq. (9). For the simulation the cuboid model is parameterized the same way as the real specimens. The thermal conductivities used as input parameters for the simulation model are shown in Table 6. The results for the thermal conductivity can be seen in Table 7. A resolution of 128^3 turned out to be sufficient for the thermal conductivity simulations. For instance, for the virtual re-grained GS14 microstructures, for 256^3 and 512^3, conductivities of 0.306W $m^{-1} K^{-1}$ and 0.314W $m^{-1} K^{-1}$ were computed, which only slightly differ in the second significant digit.

The results of the simulations on the virtually generated microstructures, cf. Table 7, overestimate the experimental data. The reason might be found in the experimental procedure, because crushed specimens were used. To accommodate for that, a second set of simulations was carried out on the virtually re-grained structures, leadin to a higher accuracy of the predicted thermal conductivities. The remaining error is probably caused by the different grain size distributions used for the simulation and the experiment. Indeed, the virtually re-grained structures are based on the un-crushed and the experimental results on the crushed specimens. The trend of the simulation results to overestimate the heat conductivities measured in the experiments could be explained by the contact conditions and the structure of the sand grains during the simulation. Whereas for the simulation, the sand grains do not vary their position and change their contact surfaces between different sand grains, in the experimental results, for each measurement a specimen has to be prepared which inevitably leads to different contact conditions and structures between the sand grains. Therefore, also a loss of contact pressure is possible which could lead to lower heat conductivities measured in the experiment.

4.3. Permeability analysis

Permeability measurements were conducted as specified in Section 3.4. The results of five different experiments are shown in Fig. 12(a). A certain degree of scattering is apparent from the data. However, the lines of best best almost coincide for 4 of the 5 experiments, emphasizing the robustness of the experimental approach.

For comparison, numerical simulations were conducted, as specified in Section 2, both on the μCT image and computer-generated structures. For the generated structures, simulations were conducted for resolutions of 128^3, 256^3 and 512^3. As for the thermal conductivity, the computed results change only on the second significant digit which is much less than the stochastic variation. Thus, we show the results computed on 512^3. The results are compared to the experimental data, cf. Fig. 12 b. The simulations

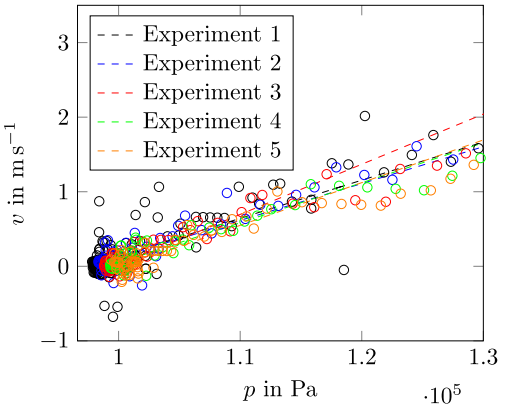

(a) Five experiments with H32 silica-sand. Circles indicate experimental values, the lines of best fit are dashed.

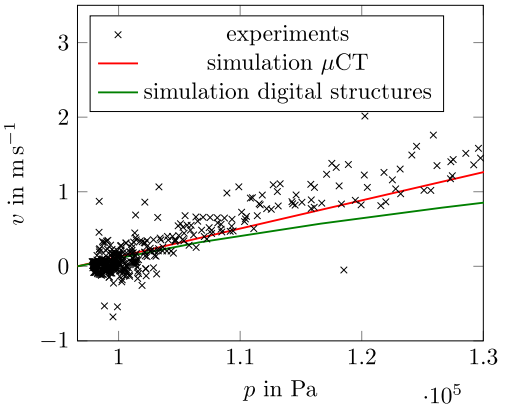

(b) Comparison of experimental data (crosses) to simulation of Stokes' flow on microstructures.

Fig. 12. Pressure-velocity curves: experimental and simulated data.

Table 6
Material parameters for thermal conductivity of SiO_2, Al_2O_3 and water glass.

	H32 (SiO_2)	GS14 (SiO_2)	W65 (Al_2O_3)	Water glass
κ / W m^{-1} K^{-1}	1.3 (Silica - silicon dioxide)	1.3 (Silica - silicon dioxide)	0.425 (Recknagel and Dahlmann)	1.36 (Silica - silicon dioxide)

Table 7
Predicted heat conductivities in W m^{-1} K^{-1} for different sands at $T = 50$°C.

Sand	H32	GS14	W65
CT	0.327	×	×
Virtual	0.413	0.432	0.171
Virtual Re-grained	0.274	0.291	0.139
Experiment	0.255	0.261	0.127

on the μCT data predict higher permeabilities than the results using generates microstructures. Still, both simulation results match the experimental data well in the range from $1.0 \cdot 10^5$ to $1.1 \cdot 10^5$Pa.

For pressures exceeding $1.1 \cdot 10^5$Pa, the simulation results based on the μCT image-segmentation lead to a better prediction of the measured permeabilities than the results using the digital structures. Still, both underestimate the permeabilities measured in the experiments. For even higher pressure, experiments show a strong non-linearity of the flow-velocities, leading to differing permeabilities. Reuß and Ratke (2010) speculate that this behavior is caused by the debonding of sand grains. We assume that this effect results from turbulence in the specimen caused by the high flow velocities in the pore space present at high pressure.

4.4. Mechanical property analysis

In this section, the results of the structural simulation for the fracture stress are compared to those of three-point bending experiments with H32 bending bars. The continuum damage model specified in Section 2.4 is solved on ten different microstructures, each of them discretized by 128^3 voxels. Unless a suitable nonlocality is introduced, the predictions of local damage models are only reliable for the resolution it has been calibrated on.

The model was calibrated on a single 128^3 microstructure. Uniaxial strain loading is monotonically increased up to a strain level of $\epsilon_{xx} = 10^{-3}$. Due to the exponential softening, the effective stress-strain-curve has a local maximum. We regard this maximum stress $\sigma_{\max}$ as the point of structural failure. To determine the parameter β, we vary β in the range $\beta \in (40, 480)$ for the simulations, as shown in Fig. 13. As expected, increasing β decreases the failure stress of the composite. To turn this discrete relationship into a continuous functional form, we make a power-law ansatz $\sigma_{\max} = c_0 \beta^{c_1}$ and identify the parameters $c_0 = 241$MPa and $c_1 = -0.76$ by regression. The resulting fit is very accurate for $\beta \geq 100$.

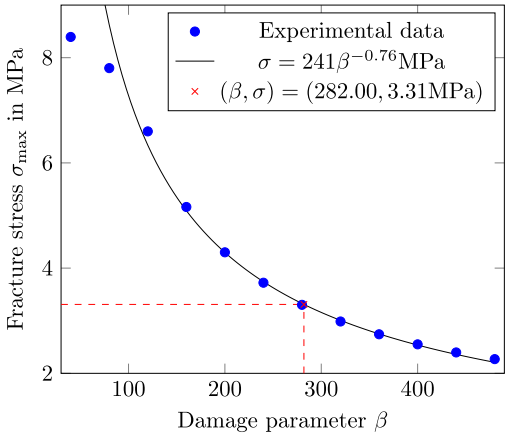

Fig. 13. Interpolation of the simulation data for different damage parameters. Evaluation for $\sigma_{\max} = 2.8$.

Using this curve, the non-observable parameter β can be identified. In the following, we wish to calibrate the modeled microscopic test volume to the fracture stress of the test specimen with 1.5 % binder. The resulting macroscopic stress is calculated according to Eq. (14). In the experiment, the nominal strength σ_N is identified as 2.88 MPa and the shape factor m reads 25.52. As we compare two different volumes ($22.8 \times 22.8 \times 175mm^3$ in experiment vs. $1.0 \times 1.0 \times 1.0mm^3$ in simulation), we rescale the nominal strength according to Eq. (19), resulting in $\sigma_N = 3.31$MPa. The calibration with $\sigma_N = 3.31$MPa leads to $\beta = 282.00$.

In Fig. 14, the four different binder volume fractions 0.5 %, 1.0 %, 1.5 % and 2.0 % are considered for a resolution of 128^3 voxels. Statistical variation is introduced in the model by working on ten different realizations for each combination, resulting in $4 \times 10 = 40$ simulations. These are used to determine emprical distributions,

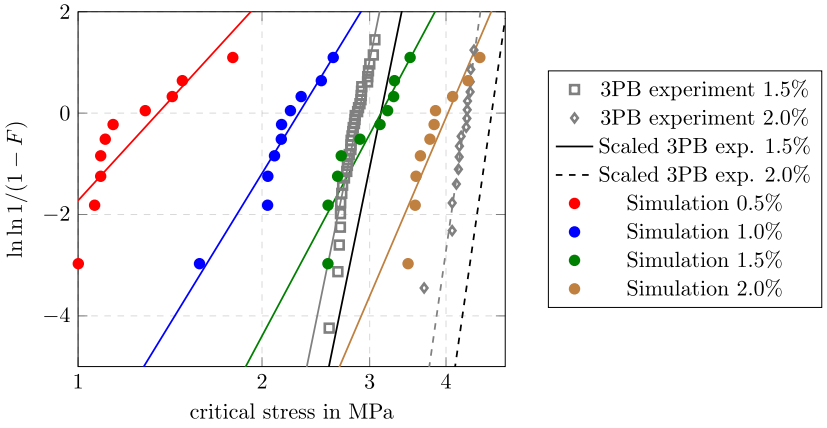

Fig. 14. Weibull plot of the failure probability F vs. critical stress comparing simulation results and three-point bending data.

Table 8
Shape and scale factors for the Weibull plots in Fig. 14.

Type	Hardened binder fraction (volume)	0.5 %	1.0 %	1.5 %	2 %
Experiment	m	x	x	25.52	36.36
	σ_N in MPa	x	x	2.88	4.31
Experiment	m	x	x	25.52	36.36
(down-scaled)	σ_N in MPa	x	x	3.31	4.75
Simulation	m	5.72	8.55	9.81	12.19
	σ_N in MPa	1.35	2.30	3.13	4.03

cf. Section 3.5, which are then compared to down-scaled three-point bending experiments with 1.5 % and 2 % hardened binder volume fraction. For the reader's convenience, the results of the three-point bending experiment are included in Fig. 14. Notice, however, that they consider a different *volume*, and are thus marked in grey. The probability distributions predicted by rescaling according to Eq. (19), accounting for the change in volume, are shown in black.

For fixed binder volume fractions, the simulated failure probabilites of the ten realizations obey a Weibull distribution, as well. Thus, the statistics of the geometrical positioning of the grains within the microstructure may offer an explanation for the failure probability being Weibull-distributed. Furthermore, this result confirms the correctness of the packing algorithm used for microstructure generation, because the two-point statistics of the sand grains appears to be correct.

The results for the Weibull fits are shown in Table 8. For the simulated data, higher binder volume fractions lead to higher nominal strengths. However, the nominal strength is underestimated for the simulations, in general. For increasing binder volume fraction, also the shape factor m increases. Practically, this reflects in a decreased variance for increasing binder content. This result confirms intuition - for low volume fraction, weak links are expected to form more easily. Still, the variance in simulation is much smaller than for the down-scaled macroscopic bending tests. Quantitatively, for both 1.5% and 2.0% binder volume fraction, the shape factors are roughly twice as high for the (down-scaled) experiment compared to the computational model. This may indicate that even larger volumes need to be simulated to better reduce the variance.

5. Conclusions

In this work, we have established a complete simulation chain for modeling the physical properties of sand cores which are of most practical interest. Starting from the individual sand grains, taking into account their specific shapes and sizes, complex three-dimensional models of the sand core microstructures were generated, which themselves served as the computational domains for numerical upscaling techniques. More specifically, we investigated thermal conductivity, gas permeability and mechanical strength, both from a simulative and an experimental point of view with modern state-of-the-art techniques.

Comparing the results led to a reasonable agreement, which is expected to improve if the material behavior of both sand grains and binder is characterized more accurately. For instance, we did not account for the cracks initially present within a sand grain. Furthermore, as a result of the shrinking during drying the binder itself may not be considered homogeneous anymore.

The results presented in this paper already provide a valid rough estimate of the composite properties. For a more precise prediction of the expected properties of sand cores, in further research the results presented in this paper need to be validated with a higher number of specimens, improving the statistical prediction.

Our approach is expected to aid in the digitalization of foundry applications, where - as for any other industrial branch - new trends in the market need to be translated into specific products quickly. More precisely, the sand type, binder volume fraction and the processing parameters should be chosen to optimize a user-defined cost-functional, for instance putting an emphasis on quality or minimizing cost.

Acknowledgements

This research was supported by DFG projects AN 341/9-1 and VO 1487/16-1. MS is partially supported by the German Research Foundation (DFG) within the International Research Training Group "Integrated engineering of continuous-discontinuous long fiber reinforced polymer structures" (GRK 2078).

We thank Franz Schreiber, Michael Godehardt, Katja Schladitz (Department of Image Processing, Fraunhofer ITWM Kaiserslautern) for the μCT-scans and the particle segmentation, Dominik Grund (Fraunhofer IGCV Augsburg) for the measurements regarding the thermal analysis and Felix Ernesti (KIT ITM) for a careful reading of the manuscript.

References

Andrä, H., Combaret, N., Dvorkin, J., Glatt, E., Han, J., Kabel, M., Keehm, Y., Krzikalla, F., Lee, M., Madonna, C., Marsh, M., Mukerji, T., Saenger, E.H., Sain, R., Saxena, N., Ricker, S., Wiegmann, A., Zhan, X., 2013. Digital rock physics benchmarks - part I: Imaging and segmentation. Comput. Geosci. 50, 25–32.

Andrä, H., Combaret, N., Dvorkin, J., Glatt, E., Han, J., Kabel, M., Keehm, Y., Krzikalla, F., Lee, M., Madonna, C., Marsh, M., Mukerji, T., Saenger, E.H., Sain, R., Saxena, N., Ricker, S., Wiegmann, A., Zhan, X., 2013. Digital rock physics benchmarks - part II: Computing effective properties. Comput. Geosci. 50, 33–43.

Baumann, T., Zunft, S., 2015. Properties of granular materials as heat transfer and storage medium in CSP application. Solar Energy Mater. Solar Cells 143, 38–47.

Chen, S.X., 2008. Thermal conductivity of sands. Heat Mass Transfer 44 (10), 1241–1246.

Coviello, A., Lagioia, R., Nova, R., 2005. On the measurement of the tensile strength of soft rocks. Rock Mech. Rock Eng. 38 (4), 251–273.

Cundall, P.A., 1988. Formulation of a three-dimensional distinct element model-part I: A Scheme to detect and represent contacts in a system composed of many polyhedral blocks. Int. J. Rock Mech. 25 (3), 107–116.

Cundall, P.A., 1988. Formulation of a three-dimensional distinct element model-Part II: Mechanical calculations for motion and interaction of a system composed of many polyhedral blocks. Int. J. Rock Mech. 25 (3), 117–125.

Danzer, R., Supancic, P., Pascual, J., Lube, T., 2007. Fracture statistics of ceramics – Weibull statistics and deviations from Weibull statistics. Eng. Fract. Mech 74, 2919–2932.

Das, N., 2007. Modeling Three-Dimensional Shape of Sand Grains Using Discrete Element Method. University of South Florida.

de Vree, J.H.P., Brekelmans, W.A.M., van Gils, M.A.J., 1995. Comparison of nonlocal approaches in continuum damage mechanics. Comput. Struct. 55 (4), 581–588.

Feyel, F., Chaboche, J.-L., 2000. FE2 Multiscale approach for modelling the elastoviscoplastic behaviour of long fibre SiC/Ti composite materials. Comput. Method. Appl. Mech. Eng. 183 (3), 309–330.

Foundry sands. https://www.strobel-quarzsand.de/Produkte_en/Giessereisand_en.html. Accessed: 2019-08-23.

Fraunhofer ITWM, Department of Image Processing, 2005. MAVI – modular algorithms for volume images. http://www.mavi-3d.de.

Fraunhofer ITWM, Department of Image Processing, 2009. ToolIP – tool for image processing. http://www.itwm.fraunhofer.de/toolip.

Fraunhofer ITWM, Department of Image Processing, 2013. MAVIkit – MAVI toolbox for ToolIP. http://www.itwm.fraunhofer.de/toolip.

GeoDict 2019. Math2Market GmbH, 2019. http://www.math2market.com.

Grassl, P., Jirásek, M., 2006. Damage-plastic model for concrete failure. Int. J. Solid. Struct. 43 (22–23), 7166–7196.

Griebel, B., Brecheisen, D., Ramakrishnan, R., Volk, W., 2016. Optical measurement techniques determine Young's modulus of sand core materials. Int. J. Metalcast. 10 (4), 524–530.

Horai, K., Simmons, G., 1971. Thermal conductivity of rock-forming minerals. J. Geophys. Res. 76 (5), 1278.

Klein, C.A., 2009. Characteristic strength, weibull modulus, and failure probability of fused silica glass. Opt. Eng. 48 (11), 113401.

Köbler, J., Schneider, M., Ospald, F., Andrä, H., Müller, R., 2018. Fiber orientation interpolation for the multiscale analysis of short fiber reinforced composite parts. Comput. Mech. 61 (6), 729–750.

Lechner, P., Stahl, J., Ettemeyer, F., Himmel, B., Tananau-Blumenschein, B., Volk, W., 2018. Fracture statistics for inorganically-bound core materials. Materials 11 (11), 2306.

Linden, S., Wiegmann, A., Hagen, H., 2015. The LIR space partitioning system applied to the Stokes equations. Graph. Model. 82 (C), 58–66.

Lubliner, J., Oliver, J., Oller, S., Oñate, E., 1989. A plastic-damage model for concrete. Int. J. Solid. Struct. 25 (3), 299–326.

Martinsen, W.E., 1969. Selected Properties of Sodium Silicate Glasses and Their Structural Significance. Iowa State University of Science and Technology.

Maurer, C.R., Qi, R., Raghavan, V., 2003. A linear time algorithm for computing exact Euclidean distance transforms of binary images in arbitrary dimensions. IEEE Trans. Pattern Anal. Mach.Intell. 25 (2), 265–270.

Mavko, G., Mukerji, T., Dvorkin, J., 2009. The Rock Physics Handbook. Cambridge University Press.

Mazars, J., Pijaudier-Cabot, G., 1989. Continuum damage theory - application to concrete. J. Eng. Mech. 115 (2), 345–365.

Midttomme, K., Roaldset, E., 1998. The effect of grain size on thermal conductivity of quartz sands and silts. Petroleum Geosci. 4 (2), 165–172.

Mollon, G., Zhao, J., 2012. Fourier-Voronoi-based generation of realistic samples for discrete modelling of granular materials. Granular Matter 14, 621–638.

Mollon, G., Zhao, J., 2014. 3D Generation of realistic granular samples based on random fields theory and Fourier shape descriptors. Comput. Methods Appl. Mech. Engrg. 279, 46–65.

O'Sullivan, C., 2011. Particle-based discrete element modeling: geomechanics perspective. Int. J. Geomechan. 11 (6), 449–464.

Pabst, W., Gregorová, E., 2013. Elastic properties of silica polymorphs a review. Ceramics-Silikaty 57 (3), 167–184.

Perras, M.A., Diederichs, M.S., 2014. A review of the tensile strength of rock: concepts and testing. Geotech. Geologic. Eng. 32 (2), 525–546. doi:10.1007/s10706-014-9732-0.

Polzin, H., 2013. Anorganische Binder: Zur Form- und Kernherstellung in der Gießerei. Schiele & Schön GmbH.

Provis, J.L., Yong, C.Z., Duxson, P., van Deventer, J.S., 2009. Correlating mechanical and thermal properties of sodium silicate-fly ash geopolymers. Colloid. Surf. A 336 (1–3), 57–63.

Quartz Sand Haltern plant H31 - H35. https://www.quarzwerke.com/en/for-customers/declaration-of-performance/. Accessed: 2019-08-26.

Rao, T.R., 1996. Metal Casting ; Principles and Practice. New Age International Publisher.

Recknagel, U., Dahlmann, M.,. Special Sands - Base Materials for State-of-the-Art Cores and Moulds. https://www.huettenes-albertus.com/fileadmin/HA_Redaktion_Datenpool/Downloads/Artikel_und_Fachvortrage/Special_Sands.pdf. Accessed: 2019-08-23.

Redenbach, C., Schladitz, K., Vecchio, I., Wirjadi, O., 2014. Image analysis for microstructures based on stochastic models. GAMM-Mittelungen 37, 281–305.

Reuß, M., Ratke, L., 2010. On the fraction of sand grains bounded in molding materials - a new measurement technique. Giessereiforschung 62 (1), 24.

Schneider, M., Hofmann, T., Andrä, H., Lechner, P., Ettemeyer, F., Volk, W., Steeb, H., 2018. Modelling the microstructure and computing effective elastic properties of sand core materials. Int. J. Solid Struct. 143, 1–17.

Schüler, T., Jänicke, R., Steeb, H., 2016. Nonlinear modeling and computational homogenization of sphalt concrete on the basis of XRCT scans. Construct. Build. Mater. 109, 96–108.

Shanthraj, P., Svendsen, B., Sharma, L., Roters, F., Raabe, D., 2017. Elasto-viscoplastic phase field modelling of anisotropic cleavage fracture. J. Mech. Phys. Solid. 99, 19–34.

Silica - silicon dioxide (sio2). https://www.azom.com/properties.aspx?ArticleID=1114. Accessed: 2019-02-27.

Spahn, J., Andrä, H., Kabel, M., Müller, R., 2014. A multiscale approach for modeling progressive damage of composite materials using fast Fourier transforms. Comput. Method. Appl. Mech.Eng. 268, 871–883.

Sutherland, W., 1893. LII. The viscosity of gases and molecular force. London, Edinburgh Dublin Philosoph. Mag. J. Sci. 36 (223), 507–531.

Tek, F.B., Dempster, A.G., Kale, I., 2005. Blood cell segmentation using minimum area watershed and circle radon transformations. In: Ronse, C., Najman, L., Decencière, E. (Eds.), Mathematical Morphology: 40 Years On. Springer Netherlands, Dordrecht, pp. 441–454.

Vergnano, A., Brambilla, E., Bonfiglioli, G., 2019. Efficiency and reliability of gravity die casting models for simulation based design. In: Advances on Mechanics, Design Engineering and Manufacturing II. Springer, pp. 3–12.

Vincent, L., Soille, P., 1991. Watersheds in digital spaces: an efficient algorithm based on immersion simulation. IEEE Trans. Pattern Anal. Mach. Intell. 13 (6), 583–598.

Wang, X., Schumacher, P., Stauder, B., 2014. Thermal physical and mechanical properties of raw sands and sand cores for aluminum casting. https://pure.unileoben.ac.at/portal/files/1913494/AC12180044n01vt.pdf. Accessed: 2019-08-23.

Wiegmann, A., 2007. Computation of the permeability of porous materials from their microstructure by FFF-Stokes. Berichte des Fraunhofer ITWM 127, 1–24.

Wiegmann, A., Zemitis, A., 2006. EJ-HEAT: a fast explicit jump harmonic averaging solver for the effective heat conductivity of composite materials. Berichte des Fraunhofer ITWM 94, 1–21.

Woodside, W., Messmer, J.H., 1961. Thermal conductivity of porous media. I. unconsolidated sands. J. Appl. Phys. 32 (9), 1688–1699.

Zych, J., Mocek, J., Snopkiewicz, T., Jamrozowicz, 2015. Thermal conductivity of moulding sand with chemical binders, attempts of its increasing. Arch. Metall. Mater. 60 (1), 351–357.